CZECH TECHNICAL UNIVERSITY IN PRAGUE

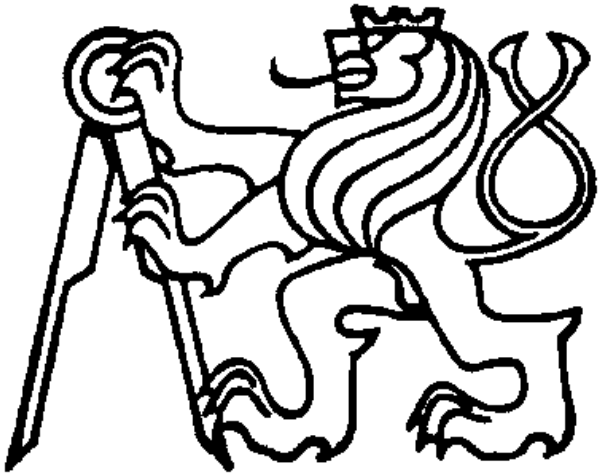

DOCTORAL THESIS STATEMENT

Czech Technical University in Prague

Faculty of Electrical Engineering

Department of Electromagnetic Field

Ing. Michal Šimůnek

PROPAGATION CHANNEL MODELING FOR LOW ELEVATION LINKS IN URBAN AREAS

Ph.D. Programme: Electrical Engineering and Information Technology

Branch of study: Radioelectronics

Doctoral thesis statement for obtaining the academic title of "Doctor", abbreviated to "Ph.D."

Prague, *August 2013*

The doctoral thesis was produced in full-time manner Ph.D. study at the Department of Electromagnetic Field of the Faculty of Electrical Engineering of the CTU in Prague

Candidate: Ing. Michal Šimůnek
Department of Electromagnetic Field
Faculty of Electrical Engineering of the CTU in Prague
Technická 2, 166 27 Prague 6

Supervisor: Prof. Pavel Pechač, Ph.D
Department of Electromagnetic Field
Faculty of Electrical Engineering of the CTU in Prague
Technická 2, 166 27 Prague 6

Consultant: Prof. Fernando Pérez-Fontán
Telecommunications Engineering School.
University of Vigo, Campus universitario,
36310 Vigo, Spain

Opponents: .....

.....

.....

.....

The doctoral thesis statement was distributed on: .....

The defence of the doctoral thesis will be held on ..... **at** ..... **before the Board for the Defence of the Doctoral Thesis in Radioelectronics in the meeting room No.** ..... **of the Faculty of Electrical Engineering of the CTU in Prague.**

Those interested may get acquainted with the doctoral thesis concerned at the Dean Office of the Faculty of Electrical Engineering of the CTU in Prague, at the Department for Science and Research, Technická 2, Praha 6.

Chairman of the Board for the Defence of the Doctoral Thesis
in Radioelectronics
Faculty of Electrical Engineering of the CTU in Prague
Technická 2, 166 27 Prague 6.

Contents

1 Introduction

Civilian applications such as air surveillance, remote sensing, and search operations are, nowadays, more often implemented by means of remote controlled Unmanned Aerial Vehicles (UAV). These aircraft are inexpensive and safe to operate. Increased demand for UAV applications correspondingly increase the need for extensive research and development. Most recent research lay in the development of hardware and software systems for developing methods for more precise and effective target acquisition in search operations [1], methods for video gathering [2] or UAV flight modeling [3], however, many of these applications need a transmission link with a ground station to immediately evaluate or store data which the control link cannot provide.

Propagation phenomena study is essential for planning and developing any link; the influence of these phenomena can then be quantified using propagation models. Many propagation models were developed for Satellite and Terrestrial links over the last few decades, however, the links for UAV communications are quite new applications and these links differ in many aspects from satellite or terrestrial links.

One of the main differences is the elevation angle which usually is at about 1 to 5 degrees. Links with this type of geometry can be classified as âĂIJLow Elevation LinksâĂİ. Another significant difference is the geometrical configuration of the transmitter and receiver where the transmitter is in motion in a homogeneous environment while the receiver is set in a static position in the middle of the scattering environment. For this type of link no propagation models have yet been published, but some research has been done. For example, in [4] an analysis of signal coverage using deterministic model is presented, or, in [5] a UAV measurement and link enhancement possibilities are described. However, it can be stated that the UAV link propagation has not been properly analyzed nor were any models developed for this type of link.

The greatest need for propagation analysis and modeling is in an urban environment as it is highly inhomogeneous and many obstacles can obstruct the link. The simplified geometry of this link in urban areas is shown in Fig. 1.1.

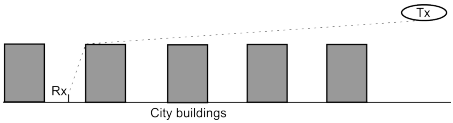

Figure 1.1: Low elevation link example

From the perspective of applications, low elevation links are considered as links with a “nomadic user”: the receiver is placed in a static position while in use, but the position can change. In this work only narrow-band mechanisms, those relevant to UAV links at UHF, will be taken into account.

The detailed analysis of known models and modeling and analyzing methods for satellite and terrestrial links can be found in full version of doctoral thesis.

2 Aims of the doctoral thesis

Expanding applications of UAV need extensive research in communication link modeling. As explained above, the corresponding low elevation link for a selected case of an urban nomadic user terminal is, from several aspects, very different from classic satellite and terrestrial links which has been investigated for decades. It is namely the geometry, movements of the elevated terminal and fixed position of the ground terminal resulting in a scenario where no relevant propagation models are available in the literature to date.

For this reason, the main goal of the thesis was defined to develop new propagation models for planning UHF narrow-band low elevation links between a slow speed UAV and a nomadic user in an urban area.

Generally there are two aspects which should be followed in wireless link planning: a model to estimate the link path loss for power budget calculations and tools to characterize the narrow-band propagation

channel. Due to the expected nature of fast fading in the urban environment, a study on space diversity would be highly appropriate. It is clear that, first, the usefulness of known modeling approaches for terrestrial and satellite wireless systems should be tested for the given scenario. However, as was shown in previous chapters, most of the available propagation models, as well as experimental datasets, are out of their validity range due to the differences in link geometry and propagation environment. It is urgent for measurement trials to provide appropriate experimental data to develop and validate the new propagation models.

The main goal of the thesis can be divided into several constituent tasks:

1. To design and conduct a propagation measurement campaign to address the given scenario of UHF narrow-band low elevation links between a slow speed UAV and a nomadic user in an urban area. The resulting experimental datasets should support the three following tasks.

2. To develop and validate the path loss propagation model for the given scenario (Chapter 3).

3. To characterize the propagation channel for the given scenario by means of both first and second order statistics and to develop and validate a corresponding time series generator (Chapter 4).

4. To analyze the space diversity gain for multiple antennas at the ground terminal for the given scenario (Chapter 5).

3 Path-loss model

The key to developing a trustworthy and widely used path-loss model is to connect the theory with measurement results by finding suitable approximations of link geometry and theory methods. A unique measurement campaign simulating an UAV by means of a remotely controlled airship was performed at 2 GHz. Based on these measurements a new path-loss model has been conducted.

3.1 Experimental trials

In this section the experiment setup is discussed, data processing is reviewed and brief comments on the results are given.

Measurement equipment

A remotely controlled airship [6] was used to simulate a UAV (Fig. 3.1). The specifications of the airship can be found in Table 3.1. The airship followed pre-defined routes carrying a transmitter while a receiver was placed in a static position on the ground. The transmitter was placed on the bottom side of the airship. The airship system also had the capability of storing pitch and roll data which were used to check the values of pitch/roll angles for the eventual discarding of invalid data. During the flights, GPS position data were stored.

Figure 3.1: Remotely controlled airship used in measurements

Length	9 m
Maximal diameter	2.3 m
Volume	27 m^3
Propulsion	electrical 2 x 700 W @ 24 V
Maximum flight level	1000 m
Maximum flight time	60 min
Flight speed	3 to 10 m/s
Maximum payload	5.5 kg

Table 3.1: Airship specifications

A transmitter, developed at the Dept. of Electromagnetic Field, Czech Technical University, was used with a carrier frequency of 2 GHz and transmitted power of 27 dBm with a signal being an un-modulated carrier (CW). A quarter-wave monopole with rod ground plane was used as a transmitting antenna.

A four-channel receiver, whose specifications can be found in Table 3.2, for performing diversity studies was setup. The receiver was also developed at the Dept. of Electromagnetic Field, Czech Technical University, connected to four monopoles, similar as at the transmitter side, forming a square with 22.5 cm sides (1.5λ). The antennas were placed 1.5 m above street level (Fig. 3.2). In this chapter, data from a single antenna are analyzed. However, consistency checks between the path-loss values measured in all four channels were carried out to verify the accuracy of the measurements.

Input frequency	1990 to 2010 MHz
Number of channels	4
Itermediate frequencies	455 MHz / 10.7 MHz
Resolution bandwidth (HPBW)	12.5 kHz
Samples per second per channel	100
Calibrated linear dynamic range	-35 to -126 dBm
Resolution of measurement	0.1 dB
Immunity to image frequency	$>$ 90 dB
Immunity to intermediate frequency	$>$ 90 dB
SSB phase noise	-100 dBc/Hz (20 kHz offset)
frequency stability	$\pm$ 1 ppm (-20° C to $+70^\circ$)
External power supply	10 to 18 V (18W)
Interface	USB

Table 3.2: Receiver specifications

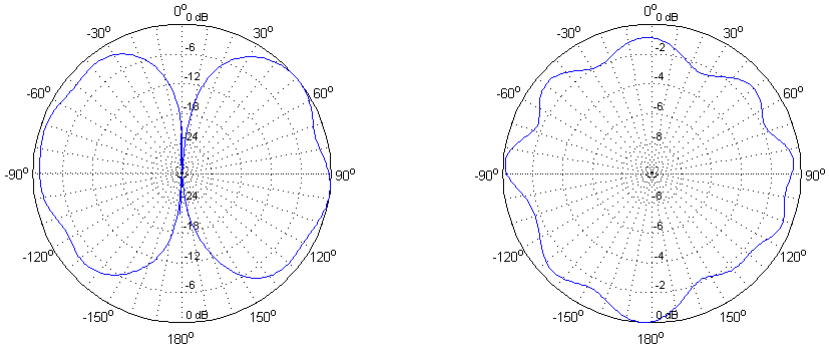

(a) (b)

Figure 3.3: Vertical (a) and horizontal (b) pattern of one antenna in the diversity array

Figure 3.2: Receiving antenna arrangement at street level.

Attention was also paid to the issue of possible mutual coupling between the antennas giving rise to distortions in the individual antenna radiation patterns. To analyze this possible issue a measurement of antenna radiation pattern in an anechoic chamber was performed. In Fig. 3.3 the vertical and horizontal pattern of one antenna in the diversity array is depicted.

It is clear that the perfectly omni-directional pattern is slightly distorted showing peak-to-peak oscillations below 3 dB. However, due to a transmitter movement within limited azimuth angles, these oscillations do not affect the received power.

Measurement setup

A fairly flat and uniformly built-up district of the Dejvice neighborhood of the city of Prague was chosen. The area is approximately 570x580 m^2 in size, buildings are of a similar type, made of brick, of about 22 m in height, built in 1922. Street widths are in the order of 17 m.

The airship flew from and toward the receiver at approximately constant azimuths from a distance of 1.2 to 6.5 km in flight levels from 150 m to 300 m above ground (Fig. 3.4 (a)). Thus, the elevation angles were from 1.6 to 6.5 degrees. The receiver was placed at two different, representative locations simulating possible positions of the UAV receiving station (Fig. 3.4 (b)).

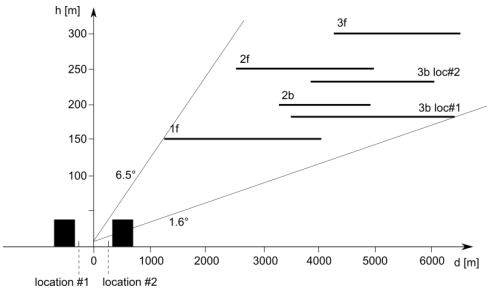

(a)

(b)

Figure 3.4: Flight and receiving antenna locations used in this study (a) and Receiver locations #1 and #2 (image from Google Earth), in Dejvice, city of Prague (b)

Data processing

First all data sources were synchronized to the GPS time and position data were enhanced using system CZEPOS [7] raising accuracy up to 0.4 m. Next invalid data due to large pitch or roll values were flagged out.

For the average path-loss analysis the fast, multipath-induced variations were removed by low pass filtering. A running mean filter was used with window size of 4,000 wavelengths (600 m). Finally, the total path loss was calculated from which the free space loss (FSL) was subtracted to calculate the excess loss, L (dB). Fig. 3.5 illustrates a path loss series as a function of the distance from the receiver for test flight 1f, Rx location #2 (Fig. 3.5).

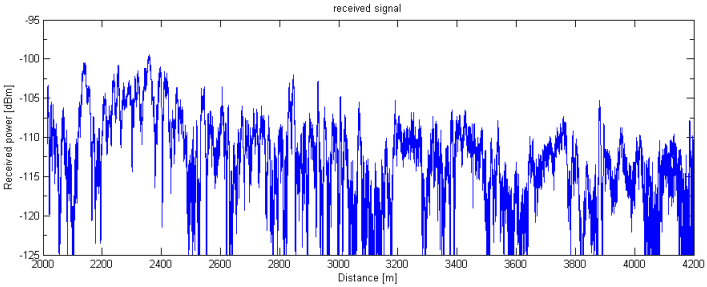

Figure 3.5: Example of path loss series as a function of distance for test flight 1f, Rx location #2

Results

Significantly strong variations due to specular reflections were observed, especially between 2 and 2.2 km (Fig. 3.5 and Fig. 3.6), and to diffuse multipath throughout. These variations suggest that the received signal is composed of several strong rays rather than from many weaker ones. Therefore, a consideration of diffuse scattering from the rear building was omitted.

A fairly distance-independent trend can be observed. Standard terrestrial empirical models like Hata-COST 231 are strongly dependent on the distance; this makes this type of model not particularly suitable for use in low elevation links such as those found in UAV applications. The data taken at location #1 (Rx on the Tx opposite side of the road) also confirmed the above observations.

Fig. 3.6 also illustrates measured excess loss after low-pass filtering for the path loss series shown in Fig. 3.5. This figure also shows modeling results which will be discussed later

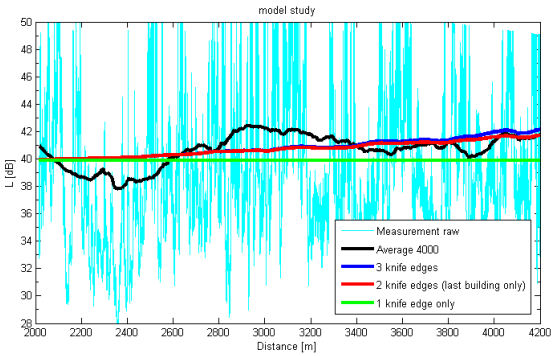

Figure 3.6: Model and measured data (row excess loss and filtered), location #2, flight 1f.

3.2 New excess loss model

Basic approach

To find a suitable method to model the excess loss, the physical mechanisms involved were considered. The main factor influencing the excess loss is diffraction. Following the well known COST 231 Walfisch-Ikegami model [8], the propagation path between transmitter and receiver can be broken down into two parts, each being affected by different diffraction mechanisms. Also in the proposed model, initially, the total contribution is divided into two components: the diffraction loss due to the last building, L_{lb}, and the diffraction loss due to the various buildings between the transmitter and the last building, L_{rt} (roof tops), which are included the first Fresnel zone. Each of these two components should be computed separately, the total excess loss being their sum, i.e.:

$$L_t(dB) = L_{lb} + L_{rt} \tag{3.1}$$

This approach is used in several semi-empirical models such as the Flat Edge Model by Saunders [9], the Walfisch-Bertoni model [10], or the already mentioned Walfisch-Ikegami (COST 231) model.

Path-loss due to the last building

UAV links are unique in the short distances from the receiver to the obstructing edge. Most previous works assume that the distance between receiver and obstruction, and between transmitter and obstruction (d_1, d_2, Fig. 3.7) are much larger than the obstruction height (h). In this case, d_1 is much larger than h but d_2 is usually of similar or smaller magnitude than h. Hence, the last building cannot be modeled by means of a single knife-edge obstruction located in its center. A solution which takes into account the short distances from receiver to obstruction is proposed in Rec. ITU-R P.526 [11], which suggests modeling the building by means of two knife edges on both outer walls, Fig. 3.7.

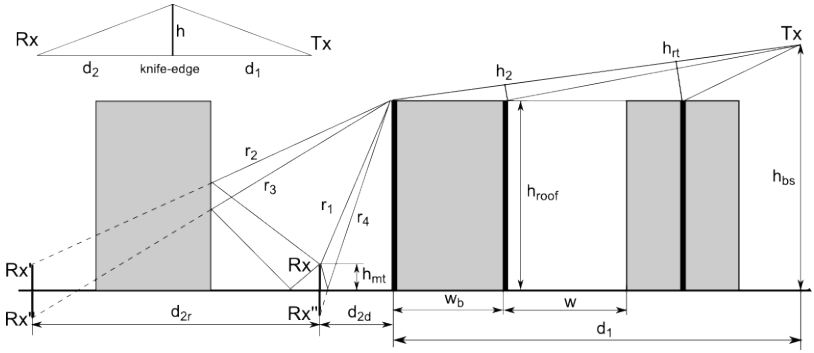

Figure 3.7: Overall propagation scenario and possible diffracted and reflected paths.

The excess attenuation due to the nearest building can be calculated using an approximate multiple knife-edge diffraction approach, Deygout's method being the optimum for the case where one edge dominates over the other [12]. This approximation identifies a main diffracting edge, the one closest to the receiver in this case, giving rise to a loss L_{lb1}. To this it is needed to add the attenuation due to the secondary knife-edge, L_{lb2}, which affects the line of sight between the top of the first knife-edge and the transmitter. The overall excess loss is thus given by

$$L_{lb}(dB) = L_{lb1} + L_{lb2} \tag{3.2}$$

So far, only one of the possible paths has been analyzed, however, the received signal at street level may be composed of many rays; of those, the most significant ones (Fig. 3.7) [13] are the direct ray (r_1) and two possible specular reflected rays, one on the building on the opposite side of the street (r_2) and another on the ground (r_4). These two contributions also undergo diffraction before being reflected. Another possible reflected contribution would be one suffering a double reflection on the building opposite and on the ground (r_3). As in [13] [14], for assessing, the excess loss can be considered as the power sum of the direct and one or more of the three reflected rays just discussed, Fig. 3.7. The general formula for the average received field, E, i.e., taking into account all possible reflections, can be expressed as a root mean square of the field strengths of components taken into consideration, as proposed Ikegami [14], i.e.,

$$E(dBV/m) = 10\log\left(\sum_{n=1}^{4} e_n^2\right) \tag{3.3}$$

The intensities in linear units are represented by lower-case letters and when in logarithmic units capital letters are used. In this paper the excess loss, L (dB), will be used instead of field strength, E, i.e.,

$$L(dB) = -10\log\left(\sum_{n=1}^{4} \frac{1}{10^{\frac{L_n}{20}}}\right) \tag{3.4}$$

Thus, the general expression for the excess loss resulting from the combination of the four rays considered, all undergoing diffraction on the closest knife-edge on the transmitter side of the street is given by

$$L(dB) = -10\log\left(\frac{1}{10^{\frac{L_1}{20}}} + \frac{r_b^2}{10^{\frac{L_2}{20}}} + \frac{r_b^2 r_g^2}{10^{\frac{L_3}{20}}} + \frac{r_g^2}{10^{\frac{L_4}{20}}}\right) \tag{3.5}$$

where the $L1$ to $L4$ (dB) are the diffraction attenuations affecting the individual rays, r_b (linear) is the magnitude of the building reflection coefficient and r_g is the magnitude of the ground reflection coefficient.

The excess loss caused by diffraction can be computed using Fresnel integrals [15]. For this geometry where the building height, h_roof, is larger than the street width, w, the normalized obstruction parameter,v, is greater than 10; in this case the following approximation of the Fresnel integrals can be used,

$$\frac{e}{e_0} = \frac{0.225}{v} \tag{3.6}$$

where e is the actual received field and e_0 is the free space under line of sight conditions. The above expression in terms of the excess loss and in dB, is given by

$$L(dB) = -20\log\left(\frac{0.225}{v}\right) \tag{3.7}$$

which shows a perfect agreement for $v > 2.5$. In general, the parameter v is defined as [11]

$$v = h\sqrt{\frac{2}{\lambda}\left(\frac{1}{d_1} + \frac{1}{d_2}\right)} \approx h\sqrt{\frac{2}{\lambda d_2}} \tag{3.8}$$

where its elements are graphically depicted in Fig. 3.7. The approximation is valid when $d_2 \gg d_1$.

As an approximation, out of the three reflected rays, only the wall reflected ray will be considered, i.e., ray r_2. Then the level and evolution of the notably slow variations is reproduced, i.e., smaller scale features have been removed. Unless the disagreement between measurements and model is unacceptable, further rays will not be introduced to keep the model simple. Also in [14] only two rays, the direct and the reflected, were considered.

For the main diffracting edge,$h \approx h_{roof} - h_{mt}$ and $d_2 \approx d_{2d} \approx d_w$, for direct ray and $d_2 \approx d_{2r} \approx (2w - d_w)$, for reflected ray (Fig. 3.7). Therefore, using (3.7) and (3.8) a final form of the last building main knife-edge attenuation L_{lb1} can be written as,

$$L_{lb1} = -10\log\left[\frac{0.05\lambda}{2(h_{roof} - h_{mt})^2}(d_w + R_b^2(2w - d_w))\right] \tag{3.9}$$

The parameters for calculating the diffraction loss due to the second edge (secondary edge) can be computed following Deygout's method (Fig. 3.7). In this case, the excess height parameter, v, for the second edge is negative. Here, a simple exponential approximation of the Fresnel Integral will be used which ignores oscillations in the field strength for $v < -1$, i.e.,

$$L_{lb2}(dB) = -20\log(1 - e^k) \tag{3.10}$$

which shows sufficient agreement for $v < 0$, and where

$$k = -0.6038 \cdot 0.1094^v \tag{3.11}$$

with v as defined in (3.8). The inverse of distance d_1, $1/d_1$, can be neglected; d_2 is represented by w_b, and h_2 (Fig. 3.7) is given by

$$h_2 \approx -w_b \sin\left(\tan^{-1}\left(\frac{h_{bs} - h_{roof}}{d - d_w}\right)\right) \tag{3.12}$$

The diffraction parameters for ray r_2 (and rays r_3 and r_4 if necessary) can be calculated in a similar way by considering the appropriate images of the receiver with respect to either the wall on the opposite side of the street or the ground.

Diffraction at multiple rooftops

For this scenario, given the low elevation angles involved, it might be necessary to take into account the additional diffraction loss introduced by the multiple buildings between the transmitter and the building nearest the receiver. This term is often found in propagation models such as the Walfisch-Ikegami (COST 231) model.

Given the geometry depicted in Fig. 3.7, where the elevation angle from the top of the last building may go from 1.4 to 5.6 degrees at most, it will be necessary to consider only one additional rooftop in the direction of the transmitter. All additional edges will introduce a negligible increase in the attenuation. Due to the large distances from the obstacle, it can be used a standard representation of the building by means

of a knife-edge in the middle of the building. In this case, the excess height, h_{rt}, will also show negative values. Thus, the same method will be used as in the second knife-edge belonging to the last building, i.e.,

$$L_{rt}(dB) = -20\log(1-e^{k}) \tag{3.13}$$

where k is defined in (3.11) and v in (8) (Fig. 3.7), h is given by

$$h_{rt} = -(1.5w_b + w)\sin\left(\tan^{-1}\left(\frac{h_{bs}-h_{roof}}{d-d_w}\right)\right) \tag{3.14}$$

the inverse distance, $1/d_1$, can be neglected and d_2 is equal to $1.5w_b + w$.

3.3 Model validation

To verify the model, the excess loss from the low-pass filtered measured data was compared with predictions using the proposed model using only rays r_1 and r_2. Already in Fig. 3.6 measured excess losses are shown for test flight 1f, Rx location#2 (closest to the nearest building). The figure also shows predictions made assuming one, two or three diffracting edges. A very good agreement between the measurements and the predictions is shown in all three diffraction configurations. However, it is clear that introducing a third diffracting edge does not improve the prediction.

In the same way, in Fig. 3.8 the same flight path for location #1 is shown (furthest from the nearest building in the direction of the transmitter). Observing both Fig. 3.6 and Fig. 3.8, a significant gain of about 5 dB can be noticed with increasing distance from the first building.

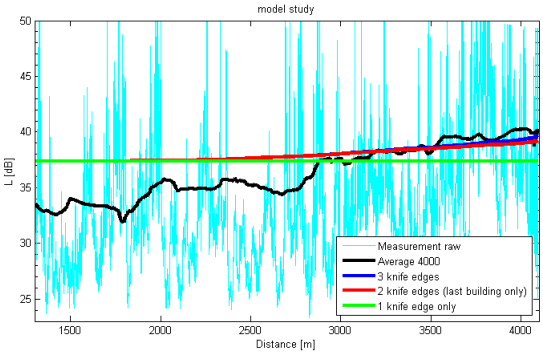

Figure 3.8: Model and measured data (raw excess loss and filtered), location #1, flight 1f.

As for the differences between predictions and measurements in Fig. 3.8, an excellent match can be observed for distances in excess of 2.5 km, i.e., for the lowest elevations in the considered range. Differences not exceeding approximately 5 dB can be observed for shorter distances, i.e., for the highest elevations in the range under study. The model predicted higher losses than the actual ones. These differences could be compensated for by including rays r_3 and r_4. However, the goal is to develop a simple model providing accurate predictions throughout the elevation angle/distance range of interest, and the accuracy achieved is acceptable. This can also be confirmed by the results in Tab. 3.3, as discussed next.

location#1	ME (dB)	STD (dB)	Path Length (m)
1f	-1.67	2.51	2810
2f	-0.42	1.35	2285
2b	1.54	2.42	1490
3f	-0.42	0.85	2154
3b	1.19	1.62	2800
Overall #1	-0.15	2.71	11539
location#2	ME (dB)	STD (dB)	Path Length (m)
1f	-0.11	0.97	2158
2f	-0.01	0.79	1719
2b	1.29	2.28	877
3f	0.09	1.26	2046
3b	0.22	1.30	2328
Overall #2	0.29	1.70	9128
Overall #1&#2	0.06	2.20	20667

Table 3.3: Comparison results with objective parameters

The values in the table show good general agreement between the measured data and model. There are deviations caused by the slow and very slow variations which cannot be predicted with this model, but the model follows the observed trend quite well in its entirety. As in Fig. 3.8, the errors become larger for the highest elevations contained in the various flight paths. However, the overall error statistics are quite good, which leads us to accept the simplest model configuration, i.e., two diffracting edges and two rays: direct and wall reflected.

4 Channel model

As in the previous chapter such research needed to be based on a valid experiment. Therefore a measurement was conducted in an urban area for analyzing and then synthesizing purposes.

4.1 Experimental trials

In this part the measurements are described. The measurement equipment was the same as in the case of path-loss modeling.

Measurement setup

For the statistical analysis, different flight route had to be set to reach a variety in received signal corresponding to the worst case scenario in the surveillance operations in urban areas. The airship followed linear routes from 1 to 6 km distances and flight levels from 100 m to 170 m above ground (Fig. 4.1 (a)). From the receiver station the UAV was seen under elevation angles from approximately 1 to 6 degrees. The configuration allowed the observation of variations in the shadowing conditions in general, fairly homogeneous. The receiver was set at three different locations (Fig. 4.1 (b)).

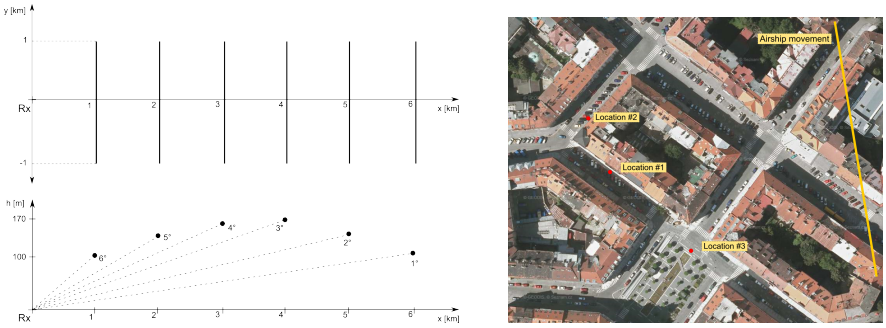

(a) (b)

Figure 4.1: Flight routes (a) and Receiver locations #1, #2 and #3 (image from Google Earth), in Dejvice, city of Prague. (b)

The expected width of Doppler spread was low given that the radius of the ring of scatterers (mainly the street-side buildings and parked cars) around the static receiver would normally be limited by the width of the street while they trace a very small angular sector (2Δ deg., Fig. 4.2) toward the moving, far away transmitter. The Doppler spread values, obtained from calculations, did not exceed a few Hz in the worst-case scenario, which, when compared with the used sampling rate of 100 Hz, allowed us ample room for capturing the deep nulls in the signal. This was so while operating within the dynamic range of the receiver. Those flight sections where the signal went below the noise threshold were discarded in the analysis. Fig. 4.2 illustrates the assumptions made in the calculations of the expected Doppler spread.

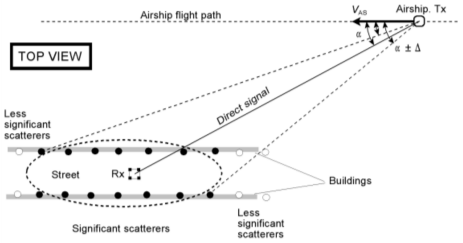

Figure 4.2: Geometry of the link to calculate the expected Doppler spread.

The Doppler shift depends on airship speed, $V_{AS} \approx 8$ m/s, transmission wavelength, $\lambda \approx 0.15$ m and the angle of the direct signal with respect to the airship's velocity vector, α deg., i.e.

$$f_{shift} = \frac{V_{AS}}{\lambda} \cos(\alpha) \tag{4.1}$$

The largest Doppler shift is observed at the ends of the nearest flight, where $\alpha \approx 45$ deg., in this case $f_{shift} \approx 37.7$ Hz.

As for the Doppler spread, a key factor in the rate of change of the fades, it is given by

$$\Delta f_{spread} = \frac{V_{AS}}{\lambda} |\cos(\alpha - \Delta) - \cos(\alpha + \Delta)| \tag{4.2}$$

Assuming that the most important scatterers are within a 50 m radius of the receiver, angle Δ for the nearest flight, at the starting point, is

$$\Delta = \tan^{-1}\left(\frac{50}{\sqrt{1000^2+1000^2}}\right) = 2.02 \quad \text{(deg.)} \tag{4.3}$$

this means that the Doppler spread in Hz is

$$\Delta f_{spread} = \frac{8}{0.15}|\cos(45^\circ - 2.02^\circ) - \cos(45^\circ + 2.02^\circ)| = 2.66 \tag{4.4}$$

It can be concluded that the available sampling rate, 100 Hz, is more than enough to capture the fading variations as their rate is driven by very small Doppler spreads.

Data processing

Unlike path-loss modeling where all fast variations in a received signal were removed by averaging, here these variations are needed for channel analysis. Hence, a path-loss is computed from received power by similar methods as in path-loss modeling, but without any averaging. Also the data were checked for high pitch and roll values. Instead of working with path-loss or excess path-loss values throughout the analysis path-gains, R and r are used, where

$$R(dB) = P_r(dBm) - P_{rFS}(dBm) \tag{4.5}$$

and

$$R(dB) = 20\log(r) \tag{4.6}$$

with P_r the actual received power in dBm, P_{rFS} the received power in dBm under free space conditions. Parameter R is the excess path gain or normalized signal level in logarithmic units, while r^2 is the path gain in linear units, where r is the received voltage normalized with respect to that of line-of-sight conditions. In the following sections the complex version of r,$\tilde{r}$, i.e. the narrow-band complex envelope will be simulated.

4.2 Statistical analysis

An example of measured path-gain series is shown in Fig. 4.3. Strong, slow variations of "arch"- like shape are observed, with each arch being approximately 30 wavelengths long. Superimposed on these slow, large-scale variations are other, faster ones. The fast variations present a small dynamic range with higher peak-to-peak excursions when they are superimposed on low level, slow-varying signals while, when the overall signal shows higher levels, the fast variations present smaller peak-to-peak ranges.

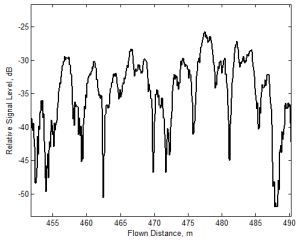

Figure 4.3: Path gain sample, location 1, Flight 3km

The geometry of this link is somewhere between that of terrestrial and LMS links. In the LMS case the received signal is assumed to be made up of the direct and multipath components. The direct component may be subjected to different levels of shadowing while the multipath component interferes with (coherently

adds to) the direct signal giving rise to fast variations. The received complex envelope can be pictured as the complex sum of two phasors: direct and multipath, i.e.

$$\tilde{r} = rexp(j\Phi) = r_D exp(j\Phi_D) + r_M exp(j\Phi_M) \tag{4.7}$$

In terrestrial links these assumptions are not used, especially in urban areas. The direct, LOS signal is normally not present and the overall received signal is assumed to be completely due to multipath whose average power changes slowly, i.e.

$$\tilde{r} = rexp(j\Phi) = r_M exp(j\Phi_M) \tag{4.8}$$

In the LMS case, different "states" or shadowing/blockage conditions are possible. In the "good state" there is normally a direct signal subjected to zero or limited shadowing effects. In the so-called "bad state", the direct signal is still present but may be comparable to or smaller than the multipath, i.e., k-factors normally below 0 dB.

An intermediate type of link was observed here where the preliminary analysis showed that negative k-factors were not very frequent. Thus, an analysis was carried out assuming that, locally, the received signal is Rice distributed with generally low k-factor values. The Rice distribution assumes the presence of a strong, coherent component plus a diffuse contribution. The coherent component, here sometimes called the direct signal, is a ray subjected to diffraction over multiple rooftops plus street-side tree shadowing.

Having made the Rice assumption, calculating the local/short-term Rice parameters by using the Method of Moments, MoM, is described in [16] as follows.

The MoM requires the signal to be windowed into sections of homogeneous characteristics so that the values of a and $2\sigma^2$ can be considered constant. There is a tradeoff between window length, which should preferably be as small as possible, and the number of samples in a window, which should be large enough to compute statistically significant parameters. It was finally observed, by trying different window sizes, that a length of 0.26 s or, equivalently, 2.08 m (assuming an average flight speed of 8 m/s) fulfilled the requirements.

Moments in this context correspond to the "moments" of the measured series, more specifically, its mean and the standard deviation. The normalized absolute value of the complex envelope is r, the normalized power is then, $p = r^2$. Two intermediate parameters are calculated, G_m and G_v, corresponding to the mean and standard deviation of p for overlapping sections or windows of 0.26 s or, equivalently, 2.08 m, i.e.

$$G_m = \text{mean}(W(p)) \tag{4.9}$$

and

$$G_v = \text{std}(W(p)) \tag{4.10}$$

where W indicates the windowing operation. The results are two series of intermediate parameters G_m and G_v values. From these the Rice distribution parameters can be calculated for the section of data inside each window, i.e.

$$a^2 = \sqrt{G_m^2 - G_v^2} \tag{4.11}$$

and

$$\gamma = 2\sigma^2 = G_m - \sqrt{G_m^2 - G_v^2} \tag{4.12}$$

The results are a series of a and γ values, representing the "local" direct signal amplitude and multipath power. Since the window slides over the original measurement, the resulting parameters are obtained with the same time/space resolution, i.e. the sampling rate. The carrier-to-multipath ratio or k-factor series is given by

$$k = \frac{a^2}{2\sigma^2} = \frac{a^2}{\gamma} \tag{4.13}$$

The above parameters in logarithmic units are as follows,

$$A(dB) = 20\log(a) \tag{4.14}$$

and

$$\Gamma(dB) = 10\log(2\sigma^2) = 10\log(\gamma) \tag{4.15}$$

where Γ and γ stand for multipath power.

Problems occur when the MoM technique is applied to very sharp signal transitions. This problem was overcome by interpolating reliable parameters on both sides of a transition, however, sharp transitions were rare. The time-series of the above two parameters was obtained from the MoM method, an example of which is shown in Fig. 4.4. analyzing the distribution of A (dB) and Γ(dB). The analysis of A yielded a sufficient fit to the normal distribution (log-normal for the amplitude of the direct signal, a, in linear units) as shown in Fig. 4.5 (a). For some flights, a better fit was found for the Rayleigh distribution (linear units, also shown in Fig. 4.5 (a) in dB). In the figure a logarithmic scale was used on the ordinate axis (probabilities) so as to have a better look at the lower tail of the distribution. The normal distribution fit is better when considering very low probability levels and then it diverges.

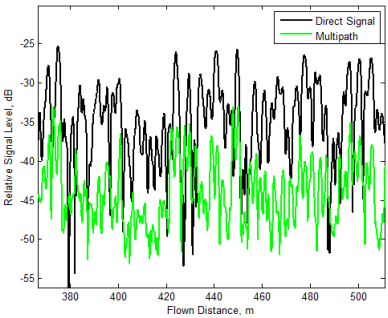

Figure 4.4: Evolution of A and Γ parameters for the time series in Fig. 4.3 (location #1, flight #3) obtained with the MoM

A log-normal distribution implies the product of numerous random attenuators, i.e., multiple diffracting rooftop edges, other elements on the rooftops, trees, etc., whereas the Rayleigh hypothesis implies the coherent sum of several (at least six or so) random phasors of approximately the same magnitude and, in general, stronger than those included in the incoherent part. In chapter 4 a path-loss model was presented where a maximum of four "stronger"/deterministic contributions may be present, as illustrated in Fig. 3.7. Which goes along with conclusions from [17]. Simple calculations have, however, shown that, at most, only two rays actually contributed significant power. Moreover, geometrically, it is difficult to explain how these contributions may be drifting in phase fast enough to give rise to fast-varying interference effects following a Rayleigh distribution.

Thus the log-normal hypothesis was pursued after verifying that the obtained results yielded a good agreement both in the first- and second-order statistics, as shown in the next section where the time-series generator is described.

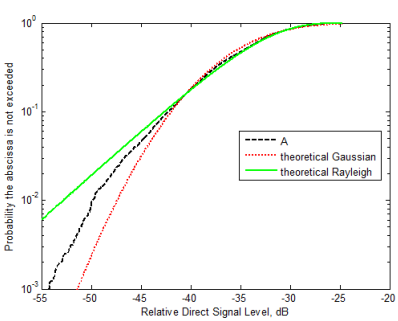

(a) Distribution of A

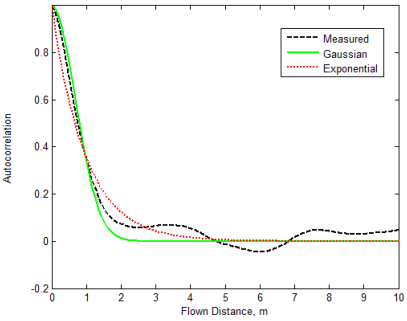

(b) Autocorrelation of A

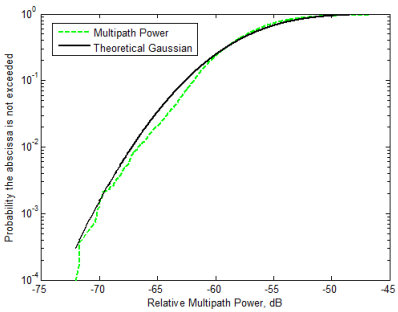

(c) Distribution of Γ

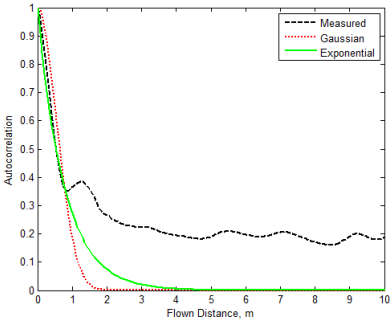

(d) Autocorrelation of Γ

Figure 4.5: Measured and fitted Gaussian and Rayleigh distributions for the variations of A (dB) (a), Measured and fitted Gaussian and exponential models for the autocorrelation in the variations of A (dB) (b), Measured and fitted Gaussian distribution for the variations of Γ (Multipath Power) (dB) (c) and Measured and fitted Gaussian and exponential models for the autocorrelation function in the variations of Γ (dB) (d) for location #1, flight #3

Then the rate of variation of A was characterized; this is given by the autocorrelation function. Fig. 4.5 (b) shows this function for one of the flights. Superimposed there are also shown a Gaussian and an exponential models. A better fit can be observed for the Gaussian model, i.e.

$$\rho_A(\Delta t) = exp\left(-\frac{\Delta t^2}{2\xi_A^2}\right) \tag{4.16}$$

where $\rho(\Delta t)$ is the autocorrelation coefficient for time-lag Δt and where ξ_A is the correlation time in the variations of A(dB). Note in Fig. 4.5 (b). how correlation times were replaced with correlation distances. The conversion between time-lags and distance-lags can be performed using the airship speed as a conversion constant. There is a particular interest in performing the study in the traveled distance domain since the speed used in the measurements may be completely unrealistic for some UAV applications. However, conversion from distance units to time units for different speeds is straightforward.

Next, the results for the time-series of Γ (dB) are presented. Like in the case of A, a fairly good fit to the Gaussian distribution was observed as exemplified in Fig. 4.5 (c) .

The fit is quite good down to the lower probability levels in the tail of the distribution. In a similar way to A, the autocorrelation function was also computed and fitted to a Gaussian model (Fig. 4.5 (d)), i.e.

$$\rho_\Gamma(\Delta t) = exp\left(-\frac{\Delta t^2}{2\xi_\Gamma^2}\right) \tag{4.17}$$

where ξ_Γ is the correlation time in the variations of Γ(dB). Again time and space are related by the airship speed, and it is more convenient to work in the distance domain as it allows extrapolation to other speeds. The fit is reasonably good at least down to a value of 0.3, including the 1/e mark where the correlation distance/time is evaluated.

Finally, the interdependence between the variations of all A and Γ was studied: the cross-correlation coefficient was relatively low, for example for location #1, flight #3, the coefficient was 0.29. This is illustrated in Fig. 4.6, where a 2D histogram of A and Γ together with a linear regression fit is shown. The slope of the fitted line is very small confirming their relatively low correlation.

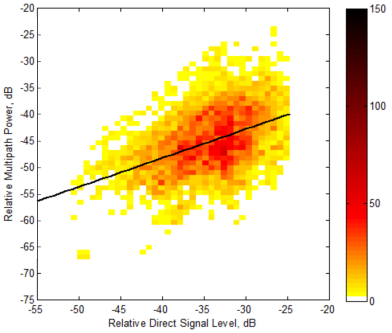

Figure 4.6: 2D histogram of A and Γ pairs (location #1, flight #3) plus regression derived straight line.

In summary, there are Gaussian variations of A and Γ characterized by their respective means and standard deviations, their rate of change can be characterized by means of Gaussian functions, but their correlation times/distances are different, i.e., they fluctuate at different rates. It was considered that A and Γ are not sufficiently correlated to introduce their mutual dependence in a simulator.

Finally, in Tab. 4.1, the ranges for the various parameters are summarized. Location 2 was excluded as the obtained parameters are similar in magnitude to those in location 1 corresponding to a street canyon situation.

Table 4.1: Time series generator parameters overview

Flight, km	location 3			location 1			
	3	4	6	3	4	5	6
ξ_A	0.848	0.876	1.700	0.678	0.912	1.018	0.863
ξ_Γ	0.453	0.396	0.679	0.540	0.460	1.004	0.848
Mean A, dB	-31.06	-31.27	-34.15	-34.89	-36.58	-38.50	-38.35
STD A, dB	4.70	4.83	4.16	4.74	4.86	4.50	3.93
Mean Γ, dB	-51.76	-52.85	-54.69	-56.80	-60.51	-62.20	-60.97
STD Γ, dB	3.36	2.65	2.18	3.78	2.77	3.22	3.26
CorrCoeff A,Γ	0.290	0.376	0.418	0.406	0.427	0.546	0.560

4.3 Time series generator

Loo model

The UAV link resembles the one found in the "bad state" LMS channel. In [18] the Loo model is proposed for its versatility for use in any possible LMS shadowing state. Thus, firstly, this model is reviewed and put in the framework of our observations.

In the Loo model[19], the received signal is assumed to vary according to a Rice distribution with parameters a and $2\sigma^2 = \gamma$. This is valid for short route sections (flight sections, in this case). For longer stretches of the route the direct signal's amplitude is assumed to vary according to a log-normal distribution, i.e.,

$$f(a) = \frac{1}{\Sigma_{Np} a\sqrt{2\pi}} exp\left[-\frac{(ln(a) - M_{Np})^2}{2\Sigma_{dB}^2}\right] = \frac{8.686}{\Sigma_{Np} a\sqrt{2\pi}} exp\left[-\frac{(ln(a) - M_{dB})^2}{2\Sigma_{dB}^2}\right] \tag{4.18}$$

where M and Γ are the mean and standard deviation of the normal distribution for the direct signal's amplitude in Nepers (ln) and in dB (20log), where the expression $ln(x) = (20/8.686)\log x$ was used for unit conversion. As in the Rice model, it assumes that the received complex envelope consists of the sum of two phasors.

The overall distribution, i.e., for longer stretches of mobile routes (flights) with homogeneous shadowing conditions, is given by

$$\begin{aligned} f(r) &= \int_0^\infty f(r|a) f(a) da \\ &= \frac{8.686r}{\sigma^2 \Sigma_A \sqrt{2\pi}} \int_0^\infty \frac{1}{a} exp\left[-\frac{r^2 + a^2}{2\sigma^2}\right] exp\left[-\frac{(20\log a - M_A)^2}{2\Sigma_A^2}\right] I_0\left(\frac{ra}{\sigma^2}\right) da \\ &= \frac{(\frac{40}{ln10})r}{\gamma^2 \Sigma_A \sqrt{2\pi}} \int_0^\infty \frac{1}{a} exp\left[-\frac{r^2 + a^2}{\gamma}\right] exp\left[-\frac{(20\log a - M_A)^2}{2\Sigma_A^2}\right] I_0\left(\frac{ra}{\gamma}\right) da \end{aligned} \tag{4.19}$$

with M_A and Σ_A in dB, and $\Gamma = 10\log(2\sigma^2)$, i.e. $\sigma = \sqrt{10^{\Gamma/10}/2}$ ($\gamma = 10^{\Gamma/10}$), is the mean squared value of the multipath component expressed in dB.

The Loo distribution is very practical as it includes, as special cases, the normal and the Rice distribution for large values of a, and the Rayleigh distribution for negligible values of a. As stated earlier, this property makes this distribution valid for a very wide range of shadowing/blockage conditions spanning from line-of-sight (LOS) to deep shadowed cases [20].

It can be observed how the Loo distribution has three parameters: M_A, Σ_A and Γ, all in dB. The first two describe the variations of A while only one parameter, Γ, the average multipath power, is used for the incoherent component. This implies that Γ does not change along the route/flight. This is in contradiction with the observations presented in the previous section.

New time-series generator

A slightly more complex model needs to be introduced to describe variations in the received signal accounting for variations in Γ or, rather, its version in linear units, γ. This requires the introduction of a second Gaussian distribution, i.e.

$$f(\gamma) = \frac{4.3429}{\Sigma\gamma\sqrt{2\pi}} exp\left[-\frac{(10\log(\gamma) - M_\Gamma)^2}{2\Sigma_\Gamma^2}\right] \quad \gamma \geq 0 \tag{4.20}$$

One further assumption, supported by observations, is the practical independence between the distributions of A and Γ, thus, the resulting distribution should come from the integration below,

$$f(r) = \int_0^\infty \int_0^\infty f(r|a,\gamma) f(a) f(\gamma) da\, d\gamma = \int_0^\infty \int_0^\infty exp\left[-\frac{r^2+a^2}{\gamma}\right] I_0\left(\frac{2ra}{\gamma}\right) \ldots$$
$$\frac{\left(\frac{20}{ln10}\right)}{a\Sigma_A\sqrt{2\pi}} exp\left[-\frac{(20\log a - M_A)^2}{2\Sigma_A^2}\right] \frac{\left(\frac{10}{ln10}\right)}{\gamma\Sigma_\Gamma\sqrt{2\pi}} exp\left[-\frac{(20\log\gamma - M_\Gamma)^2}{2\Sigma_\Gamma^2}\right] da\, d\gamma \tag{4.21}$$

The above distribution only deals with amplitudes, however, it is also necessary to reproduce the rates of change in the various parameters. This is accomplished by using several low-pass filters, as shown in the schematic diagram of the time-series synthesizer associated with the model shown in Fig. 4.7. In the diagram there are two main blocks: the top one deals with generating the diffuse component while the bottom block oversees the generation of the direct signal. The outputs of both blocks can be complex; they are finally added to generate the overall complex envelope. The magnitude of the simulated series can be derived by taking the absolute value.

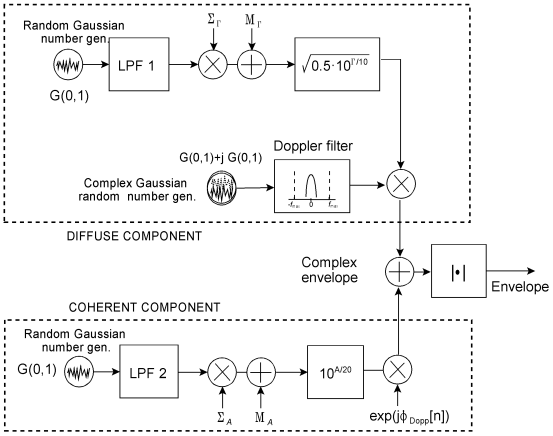

Figure 4.7: Generator scheme

The Doppler shift was introduced in the direct signal branch, which can be calculated from the link geometry since,

$$f_{\text{Doppler}} = (v/\lambda)\cos(\xi) \tag{4.22}$$

where v is the UAV speed, λ is the wavelength and ξ is the angle between the radio path and the direction of flight.

Looking now into the top block, there are two branches: the upper with a Gaussian number generator followed by a low-pass filter (LPF1) implementing the wanted autocorrelation properties. The filter is a sampled and windowed Finite Impulse Response (FIR) version of the required impulse response.

Then, the filtered series was scaled to the adequate mean and standard deviation: M_Γ, Σ_Γ, and converted to linear units using

$$\sigma = \sqrt{\frac{10^{\frac{\Gamma}{10}}}{2}} \tag{4.23}$$

to modulate the modal value, σ, of the Rayleigh generator, in the lower branch in the diffuse component block. The first step when designing the filter is the autocorrelation function, $\rho_\Gamma(\Delta t)$; its Fourier transform is the power spectral density, $S(f)$. The following assumption can be made [21],

$$H_\Gamma(f) = \sqrt{S_\Gamma(f)} \tag{4.24}$$

Thus, taking the Fourier transform of the correlation function and the square root and transforming back yield:

$$\rho_\Gamma(t) = \exp\left(-\frac{t^2}{2\xi^2}\right) \xrightarrow{F} S(f) = \xi \exp[-2(a\pi f)^2] \tag{4.25}$$

$$h(t) = \sqrt{2}\exp\left(-\frac{t^2}{\xi^2}\right) \xleftarrow{F^{-1}} H(f) = \sqrt{S(f)} \tag{4.26}$$

The sampling rate in this branch is also f_s (Hz) as in the case of the Doppler filter. The resulting impulse response is finally windowed using the Hanning window.

The lower branch of the top block is a Rayleigh series generator consisting of a complex Gaussian random number generator, each of its components (in-phase and quadrature) has zero mean and a standard deviation equal to one. The resulting complex signal, generated at a rate f_s (Hz), is filtered by means of a Butterworth filter to reproduce the Doppler spreading caused by multipath. There is no access to complex envelope measurements for computing the Doppler spectrum, however, the expected theoretical spreading from the geometry of the link is rather small, in the order of a few Hz. This means that a very narrow Doppler filter is necessary. The filter was parametrized by trial and error based on the expected Doppler bandwidth and comparing the results with the measurements. The expected Doppler bandwidth is determined by the angular sector between the transmitter and the ring of scatterers around the receiver which, most likely, are located in the same street/square the receiver is in. The radius of this ring of scatterers is much smaller that the Tx-Rx distance.

After filtering, there is a Rayleigh series of modal value equal to one. The wanted modal value is set by multiplying the resulting complex filtered signal by the output of the top branch in the incoherent component block which is a slowly varying log-normal series with Gaussian autocorrelation as discussed in the previous paragraphs.

As with the upper block, the lower block is responsible for reproducing variations in the direct/coherent component which are Gaussian in dB and show Gaussian correlation properties. Again, a filter, LPF2, for introducing the right rate of change in the variations of A must be used. The sampling rate is also f_s (Hz) as in the other branches.

As indicated above, there is an assumption that the variations of A and Γ are uncorrelated in this implementation of the simulator. As shown next, the agreement between synthesized and measured series is quite good. However, for general purposes, a comprehensive synthesizer should be able to force some degree of correlation between the two variables.

Generator validation

Several tests are presented below to illustrate the similarity of the synthesized seriesâĂŹ first and second-order statistics with respect to those of the original experimental series. The synthesizer parameters were the ones extracted from the measured series used for comparison. In Fig. 4.8 (a) a synthesized series is shown together with the original measured series. In the validation the simulator was run ten times and the corresponding statistics were plotted together with those of the measured series.

Thus, in Fig. 4.8 (b) the CDFs (Cumulative Distribution Functions) are shown for the measured and simulated series. The similarity is quite good down to the tail of the distribution. The effectiveness of the filters introduced in the modeling can be observed by comparing the LCR (level crossing rate) and AFD (average fade duration) plots. These are illustrated in Fig. 4.8 (c),(d). The deviations between the experimental and synthesized series statistics can be considered to be sufficiently small. Similar fits could be observed for other flights and measurement locations.

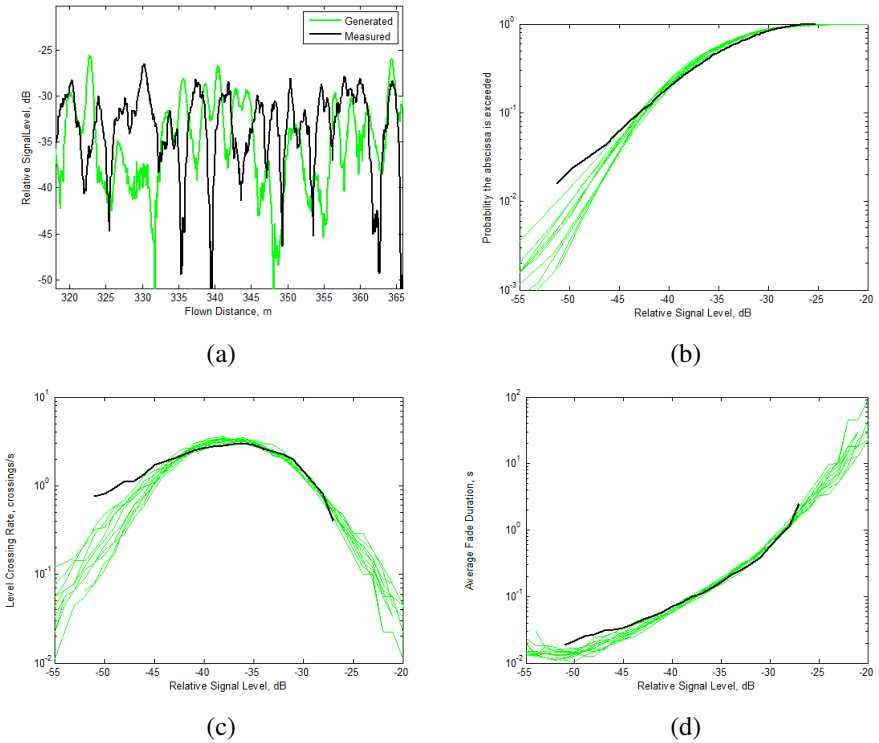

Figure 4.8: Measured and simulated series comparison in time (a), by means of CDF (b), by means of LCR (c) or by means of AFD (d) for location #1, flight #3

5 Space diversity

A study of space diversity was based on measurements from chapter 4. The processing of received power data was similar, however, signals from all four channels were used here: First, the free space level was subtracted from the measured received power series for computing the excess path gain, the inverse of the excess loss. Then, the excess path gain was converted to linear units (normalized received voltage or signal envelope) for performing signal combining. The combining was performed ad post in Matlab environment. After combining, the resulting envelopes were converted back to logarithmic units for further analysis.

Three combining methods were tested: selective combining (SC); Maximal Ratio Combining (MRC); Equal Gain Combining (EGC). The resulting envelope is denoted by r_0 and the individual branch envelopes are denoted by r_i as in [12]

For illustrative purposes location #3, flight #3 was chosen, i.e. an elevation angle of 4 deg. with the receiver located at the open square in Fig. 4.1 (b). Fig. 5.1 (a) shows a 30 m section of the 2 km flight illustrating the variations in the received signal picked up by each of the four diversity branches.

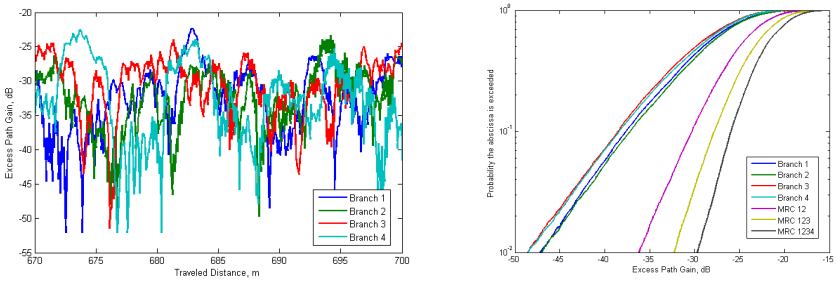

(a) (b)

Figure 5.1: Section of 30 m of the 2 km flight (a) and CDFs of original series and of incrementally MRC-combined signal (b) for the flight #3 and location #3

The cumulative distribution functions, CDFs, for the individual diversity branches are presented in Fig. 5.1 (b). From the figure it can be observed how the four branches show quite well balanced distributions. This is one of the two requirements for achieving significant diversity gains. The other requisite is low cross-correlations. Thus, the correlation between the signal envelopes in the four branches were also analyzed yielding

$$p = \begin{bmatrix} 1.00 & 0.18 & 0.09 & 0.02 \\ 0.18 & 1.00 & 0.15 & 0.03 \\ 0.09 & 0.15 & 1.00 & 0.06 \\ 0.02 & 0.03 & 0.06 & 1.00 \end{bmatrix} \tag{5.1}$$

It is clear that the four envelopes are low correlated, promising significant diversity gains. Further work regarding the evaluation of the diversity gain was performed on the measured series normalized with respect to their RMS level. Moreover, the normalized series were fitted to a Rayleigh distribution. In Fig 5.2 the CDFs of the normalized envelope in branch 1 can be found and that of the successive incremental combinations. The combined signal statistics show substantial incremental gains with higher median values and higher levels, especially for the low probability levels of exceedance. It is clear, as expected, that the main improvement is achieved when the first diversity branch is introduced and then, a law of diminishing returns is observed when additional, new branches are introduced.

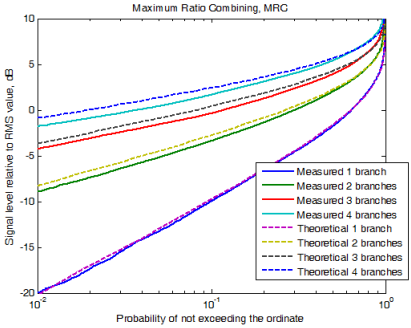

Figure 5.2: Measured and uncorrelated Rayleigh model CDFs for rms level normalized series corresponding to one banch and incremental 4-branch diversity plus MRC.

In the current case (flight and location) the fit to Rayleigh distribution was quite good indicating that the much more favorable Rice character found for higher elevations corresponding to mobile-satellite links [22] did not fully describe the link. This was the case for all flights and locations. The Rayleigh distribution satisfactorily explains the large-scale behavior of the signal. However, the small-scale, or the details, in the measured signal are somewhat different as was found in the analysis described in previous chapter.

For reference, a comparison of the measured and predicted (assuming uncorrelated Rayleigh branches) diversity gains is also present [12]. The diversity gain is defined as the dB difference for equal probability levels between the CDF of an individual branch and that of the combined signals.

From the results presented in Fig. 5.2, the incremental diversity gains assuming MRC are explicitly shown in Fig. 5.3 (a). As expected, the largest increment is achieved when introducing the first diversity branch. Further branches bring about smaller increments but, still, substantial ones, e.g. for the 1% probability level the possible gain is about 12 dB when diversity is introduced and this is incremented to about 18 dB when four branches are used. In the figure the deviation from the uncorrelated Rayleigh fading case are also illustrated , indicating, as mentioned, that the Rayleigh distribution does not explain the overall behavior of the channel.

In Fig. 5.3 (b) the CDFs obtained for SC, EGC and MRC for four-branch diversity are shown, together with the predictions from the Rayleigh model, indicating a minor improvement obtained with MRC with respect to EGC and SC at the expense of the needed additional complexity

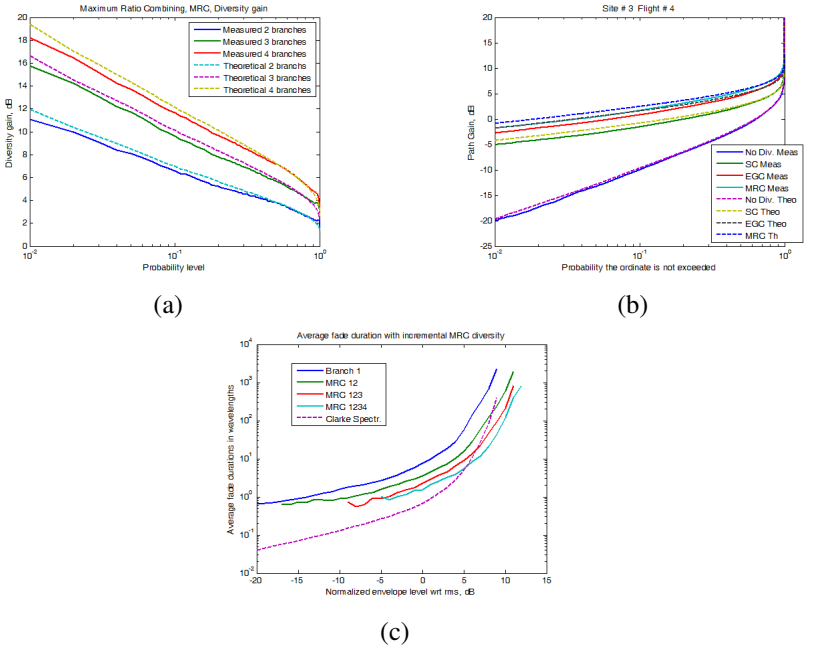

Figure 5.3: Measured and uncorrelated Rayleigh model 4-branch incremental diversity gains using MRC (a) , CDFs of all three combining methods (b) and Theoretical Rayleigh + Clarke Doppler spectrum AFD, and AFD of experimental single branch and 4-branch incremental MRC (c)

The observed behavior, diversity-wise, was similar for all elevations and locations. As for the average received power this only increases marginally with the elevation angle in an approximately 5 dB range.

Further, the implications of using diversity on a second-order statistic, the average fade duration, AFD were briefly analyzed . The durations were expressed in length of flight units and normalized then with respect to wavelength. In Fig. 5.3 (c) the afds for branch-1 and for the incrementally combined signals from

1 through 4 are shown. Also, the afd for a Rayleigh channel with Clarke Doppler spectrum [12] is shown for reference.

It is clear that, in our case, the signal variations are much slower than in the Clarke case given that the Doppler spectrum is much narrower. The introduction of MRC combining results in fades of shorter duration; this helps reduce the length of the codewords and/or interleaver depths necessary to overcome the deep and long fades encountered.

The results from this analysis were compared with the results from preliminary experiment in wooded area where the diversity gains achieved are lower but still substantial. This comparison was published in [23].

6 Conclusions

UAV systems are nowadays finding the place in many surveillance missions. For developing and testing such systems, modeling and analyzing the link between the UAV and ground receiver station is needed. The link has a geometry different from any satellite or terrestrial system in use, consequently, this does not provide a suitable solution. A full study of loss mechanisms and link statistical characteristics has to be performed and new models have to be developed, based on propagation modeling knowledge, to suit UAV applications properly.

Chosen propagation modeling methods and their approximations were adapted for UAV link specifications. For this purpose a series of measurements was conducted with an unmanned airship as a UAV and a four-channel receiver on the ground. An urban environment was chosen for the modeling and analysis as the large number of obstacles and scatterers are central to the study.

Based on the methods and approximations in correlation with a measurement comparison a new path-loss model was developed. The model uses the Fresnel Integrals approximation of diffraction on the last building before the receiver. The building shape was approximated as two knife-edges on the wall. The influence of other buildings and their rooftops was found to be negligible. The propagation in the street was modeled by a two-ray approach where one ray is direct from the last obstacle and the second is reflected from the rear building. Influence from other rays was also found to be negligible. The model was validated after comparing measurements and the developed path-loss model was published in [24].

A statistical analysis of received signal was next performed. It was found that the amplitudes are Rice distributed and the Loo model was studied for possible usage. Unlike in the Loo model, the average multipath power was observed to be independent of mean power of the direct component and varies randomly. The Doppler spread was also found to be quite narrow due to low angular changes in geometry with transmitter movement. All mechanisms were set together and a new time-series generator was developed and validated by statistical comparison with the measured data. The analysis and new time-series generator were published in [25].

After characterizing the link by means of average path-loss and fade statistics, a study of link enhancement possibilities was conducted. A four-channel space diversity was tested in the urban area and the enhancement quantified by diversity gain value. It was concluded that the channel is low correlated and significant gains can be achieved.

Based on the results it can be stated that the objectives of this work were accomplished. As the main contribution the two new propagation models were developed for planning UHF narrow-band low elevation links between a slow speed UAV and a nomadic user in an urban area.

However, this work is only the first step in the area of UAV link propagation modeling. In this work only one frequency was used, whereas higher frequencies may satisfy higher demands on data rate (for higher resolution or frame speed of video). Also other diversity techniques - polarization, frequency, angle diversity etc. - should be studied together with a full MIMO type of link using the latest research in the MIMO area for satellite and terrestrial links. Finally another scenarios can enhance the usability of model.

At this moment there is a lack of legislation for using the UAV for commercial purposes in Czech Republic. However, in non-commercial areas the UAV more often covers surveillance missions and if, in the future, UAV traffic is opened, the need for propagation modeling will significantly increase.

Bibliography

[1] H. Al-Helal and J. Sprinkle. UAV Search : Maximizing Target Acquisition. *17th IEEE International Conference and Workshops on Engineering of Computer-Based Systems*, pages 9 – 18, 2010.

[2] G. Zhou and D. Zang. Civil UAV System for Earth Observation. In *Geoscience and Remote Sensing Symposium IGARSS*. IEEE International, 2007.

[3] L. Peng and Q. Geng. Real-time simulation system for UAV based on Matlab/Simulink. In *IEEE 2nd International Conference on Computing, Control and Industrial Engineering (CCIE)*, volume 1, 2011.

[4] C. Cerasoli. An analysis of unmanned airborne vehicle relay coverage in urban environments. In *Military Communications Conference*. MILCOM 2007, 2007.

[5] J. Romeu, A. Aguasca, J. Alonso, S. Blanch, and R. R. Martins. Small UAV radiocommunication channel characterization. In *Proceedings of the Fourth European Conference on Antennas and Propagation (EuCAP)*, 2010.

[6] www.airshipclub.com.

[7] geoportal.cuzk.cz.

[8] D. J. Cichon and T. Kurner. Propagation Prediction Models, Chapter 4. Technical report, COST 231 final report, 1999.

[9] S. Saunders and F. Bonar. Explicit Multiple Building Diffraction Attenuation Function for Mobile Radio Wave Propagation. *Electronics Letters*, 27(14):1276–1277, 1991.

[10] J. Walfish and H. Bertoni. A theoretical model of UHF propagation in urban environments. *IEEE Transactions on Antennas and Propagation*, 36(12):1788–1796, 1988.

[11] ITU-R P.526-11. Propagation by diffraction. 2009.

[12] J. Parsons. *Mobile Radio Propagation Channel*. Wiley, 2nd edition, 2000.

[13] H. Bertoni. *Radio Propagation for Modern Wireless Systems*. Prentice Hall PTR, 2000.

[14] F. Ikegami, S. Yoshida, T. Takeuchi, and M. Umehira. Propagation Factors Controlling Mean Field Strength on Urban Streets. *IEEE Transactions on Antennas and Propagation*, 32(8):822–829, 1984.

[15] L. Barclay. *Propagation of Radiowaves*. IEE, 2nd edition, 2003.

[16] L. Greenstein, D. Michelson, and V. Erceg. A Moment-Method Estimation of the Ricean K-Factor. *IEEE Communications Letters*, 3(6):175–176, 1999.

[17] F. Ikegami and S. Yoshida. Analysis of multipath propagation structure in urban mobile radio environments. *IEEE Transactions on Antennas and Propagation*, ap-28(4):531–537, 1980.

[18] L. E. Braten and T. Tjelta. Semi-Markov multistate modeling of the land mobile propagation channel for geostationary satellites. *IEEE Transactions on Antennas and Propagation*, ap-50(12):1795 – 1802, 2002.

[19] Ch. Loo. A statistical model for a Land Mobile Satellite Link. *IEEE Transactions on Vehicular Technology*, vt-34(3):122 – 127, 1985.

[20] Fernando P. Fontan, A. Mayo, D. Marote, R. Prieto-Cerdeira, P. Marino, Fernando D. Machado, and N. Riera. Review of Generative Models for the Narrowband Land Mobile Satellite Propagation Channel. *International Journal of Satellite Communications*, 26:291–316, 2008.

[21] D. Young and N. Beaulieu. The Generation of Correlated Rayleigh Random Variates by Inverse Discrete Fourier Transform. *IEEE Transactions on Communications*, 48(7):1114 – 1127, 2000.

[22] R. P. Cerdeira, F. P. Fontan, P. Burzigottil, A. B. Alamanax, and I. S. Lago. Versatile two-state land mobile satellite channel model with first application to DVB-SH analysis. *International Journal of Satellite Communications Networking*, 28:291 – 315, 2010.

[23] M. Simunek, P. Pechac, and F. P. Fontan. Feasibility of UAV Link Space Diveristy in Wooded Areas. *International Journal of Antennas and Propagation*, 2013.

[24] M. Simunek, P. Pechac, and F. P. Fontan. Excess Loss Model for Low Elevation Links in Urban Area for UAVs. *Radioengineering*, 20(3):561–568, 2011.

[25] M. Simunek, F. P. Fontan, and P. Pechac. The UAV Low Elevation Propagation Channel in Urban Areas: Statistical Analysis and Time- Series Generator. *IEEE Transactions on Antennas and Propagation*, 61(7):3850 – 3858, 2013.

List of candidate's works relating to the doctoral thesis

Articles in impacted journals

[1] M. Simunek, P. Pechac, F. P. Fontan, "Excess Loss Model for Low Elevation Links in Urban Area for UAVs", *Radioengineering*, vol. 20, no. 3, pp. 561-568, September 2011. (33%)

[2] M. Simunek, F. P. Fontan and P. Pechac, "The UAV Low Elevation Propagation Channel in Urban Areas: Statistical Analysis and Time-Series Generator", *IEEE Transactions on Antennas and Propagation*, vol. 61, no. 7, pp.3850-3858, July 2013. (33%)

[3] M. Simunek, F. P. Fontan and P. Pechac and F. J. D. Otero, "Space Diversity Gain in Urban Area Low Elevation Links for Surveillance Applications", *submitted to IEEE Transactions on Antennas and Propagation Communications*, August 2013. (25%)

[4] M. Simunek, P. Pechac, and F. P. Fontan, "Feasibility of UAV Link Space Diversity in Wooded Areas," *International Journal of Antennas and Propagation*, vol. 2013, Article ID 890629, 5 pages, 2013. (33%)

Responses on [1]

Y. H. Lee, Y. S. Meng, "Empirical Modeling of Ducting Effects on a Mobile Microwave Link Over a Sea Surface", *Radioengineering*, vol. 21, no. 4, December 2012.

Articles in peer-reviewed journals

Patents

Publications listed in Web of Science

[5] M. Simunek, P. Pechac, F. P. Fontan, "Space diversity analysis for low elevation links in urban areas," *Antennas and Propagation (EUCAP), 2012 Proceedings of the Sixth European Conference on*, pp.1165-1168, 26-30 March 2012. (33%)

[6] M. Simunek, P. Pechac, F. Perez-Fontan, "Space diversity analysis for low elevation links in a wooded area," *Antennas and Propagation (EuCAP), 2013 Proceedings of the Seventh European Conference on*, pp.2336,2339, 8-12 April 2013. (33%)

Other publications

List of other publications

Articles in impacted journals

Articles in peer-reviewed journals

Patents

Publications Listed in Web of Science

[7] Horak, P.; Kvicera, M.; Simunek, M.; Korinek, T.; Zela, J.; Pechac, P., "Vegetation attenuation measurements at 2 GHz using a remote-controlled airship — Initial results," *Antennas and Propagation (EuCAP), 2010 Proceedings of the Fourth European Conference on* , pp.1,4, 12-16 April 2010. (17%)

[8] Kvicera, M.; Horak, P.; Korinek, T.; Zela, J.; Simunek, M.; Pechac, P., "Building penetration loss measurements for satellite-to-indoor systems: Preliminary results," *Antennas and Propagation (EuCAP), 2010 Proceedings of the Fourth European Conference on* , pp.1,4, 12-16 April 2010. (17%)

Other publications

Resumé

Tato práce pojednává o modelování šíření elektromagnetických vln v zástavbě pro spoje s malou elevací pro účely komunikace s bezpilotními prostředky. Systémy využívající bezpilotní prostředky (UAV) jsou v poslední době stále více využívány především pro pozorovací a vyhledávácí účely. Pro návrhy a provozování takových systémů je nezbytná znalost vlivu prostředí na šíření elektromagnetických vln pro daný spoj, resp. příslušných modelů šíření vln. Pro výše popsaný typ spoje nebyly dosud publikovány žádné modely a je tedy potřeba vyvinout modely nové, uvažující odlišnosti tohoto spoje od doposud známých satelitních či pozemních.

Byla provedena série experimentů, které umožňují porovnání teoretických předpokladů se všemi skutečnými vlivy v daném prostředí.

Na základě zkoumání dosud známých metod modelování pro satelitní a pozemní spoje a na základě konfrontace s daty z experimentů byl vyvinut nový model pro odhad útlumu způsobeného zástavbou pro spoje s malou elevací. Nový model uvažuje především difrakci na poslední budově, která byla pro jednoduchost a univerzálnost modelu zjednodušena na dvě nekonečně tenké vlny absorbující překážky (knife-edge). Difrakce je řešena pomocí Fresnelovy aproximace a pro výpočet vícenásobné difrakce je použit Deygoutův princip. V modelu se dále uvažuje že se vlna v ulici šíří především ve dvou paprscích: Přímém a odraženém od zadní budovy. Model byl porovnán s naměřenými hodnotami útlumu s dostatečnou shodou.

Dále se v práci popisuje statistický rozbor přijatého signálu a jeho frekvenční vlastnosti na jejichž základě je poté vyvinut generátor dat který zohledňuje všechny vlivy na daný signál a dokáže generovat signál se stejnými statistickými vlastnostmi. Nový generátor využívá tzv. Loo model s tím, že jsou přidány frekvenční vlastnosti druhého řádu pomocí metody filtrování Gaussovského šumu (FGN). Navíc oproti všem známým modelům zde bylo pozorováno a následně zohledněno, že amplituda složky, kterou způsobuje vícecestné šíření, je taktéž náhodná veličina.

Jako poslední je v práci věnována pozornost metodám zlepšení příjmu a potlačení úniků signálu pomocí metody diverzitního příjmu. Na základě zkoumání dat z experimentů byly prezentovány a vyčísleny možnosti diverzitního zisku pro vybrané metody.

Summary

UAV systems are nowadays finding the place in many surveillance missions. For developing and testing such systems, modeling and analyzing the link between the UAV and ground receiver station is needed. The link has a different geometry from any satellite or terrestrial system in use, consequently, this does not provide a suitable solution. A full study of loss mechanisms and link statistical characteristics has to be performed and new models have to be developed, based on propagation modeling knowledge, to suit UAV applications properly.

In this work analytical and modeling methods from satellite and terrestrial links were studied and their suitability for UAV links in urban areas was discussed. Specifically chosen methods and their approximations were then adapted for UAV link specifications. For this purpose a series of measurements was conducted with an unmanned airship as a UAV and a four-channel receiver on the ground.

Based on the methods and approximations in correlation with a measurement comparison a new path-loss model was developed. The model uses the Fresnel Integrals approximation of diffraction on the last building before the receiver. The building shape was approximated as two knife-edges on the wall. The influence of other buildings and their rooftops was found to be negligible. The propagation in the street was modeled by a two-ray approach where one ray is direct from the last obstacle and the second is reflected from the rear building. An agreement of modeled with measured data was found as acceptable.

A statistical analysis of received signal was next performed. It was found that the amplitudes are Rice distributed and the Loo model was studied for possible usage. Unlike in the Loo model, the average multipath power was observed to be independent of mean power of the direct component and varies randomly. All mechanisms were set together and a new time-series generator was developed and validated by statistical comparison with the measured data.

After characterizing the link by means of average path-loss and fade statistics, a study of link enhancement possibilities was conducted. A four-channel space diversity was tested in the urban area and the enhancement quantified by diversity gain value. It was concluded that the channel is low correlated and significant gains can be achieved.